

Kinetic magnetoelectric effect in topological insulators

Ken Osumi¹, Tiantian Zhang ^{1,2} & Shuichi Murakami ^{1,2} 

The kinetic magnetoelectric effect is an orbital analog of the Edelstein effect and offers an additional degree of freedom to control magnetization via the charge current. Here we theoretically propose a gigantic kinetic magnetoelectric effect in topological insulators and interpret the results in terms of topological surface currents. We construct a theory of the kinetic magnetoelectric effect for a surface Hamiltonian of a topological insulator, and show that it well describes the results by direct numerical calculation. This kinetic magnetoelectric effect depends on the details of the surface, meaning that it cannot be defined as a bulk quantity. We propose that Chern insulators and Z_2 topological insulators can be a platform with a large kinetic magnetoelectric effect, compared to metals by 5–8 orders of magnitude, because the current flows only along the surface. We demonstrate the presence of said effect in a topological insulator, identifying $\text{Cu}_2\text{ZnSnSe}_4$ as a potential candidate.

¹Department of Physics, Tokyo Institute of Technology, Tokyo, Japan. ²TIES, Tokyo Institute of Technology, Tokyo, Japan.
email: murakami@stat.phys.titech.ac.jp

In recent years, new responses leading to orbital magnetization have been proposed in systems without inversion symmetry^{1–18}. One of the focuses is the conversion of electron current and magnetization on crystal structure with low symmetry. Among such proposals are kinetic magnetoelectric effect (KME)^{1–3,10,11,13–15,18}, also called orbital Edelstein effect, i.e., current-induced orbital magnetization, and the gyrotropic magnetic effect^{4–6}. These effects have similar response coefficients. In particular, KME is an orbital analog of the Edelstein effect^{19–21}. KME emerges even in systems without spin-orbit interactions^{1,3}. In particular, the KME emerges in crystals with a chiral structure^{1–3}, similar to the phenomenon in which the solenoid creates a magnetic field when a current flows. In a similar context, the recent finding of spin-selective electron transport through chiral molecules, the so-called chirality-induced spin selectivity (CISS) effect^{22–26}, suggests an alternative method of using organic materials as spin filters for spintronics applications.

In the KME, the electric field induces magnetization, which may look similar to the magnetoelectric (ME) effect^{27–35}. Nonetheless, in the spin Edelstein effect and KME, metallic systems are considered, and nonequilibrium electron distribution by the electric field is a key to generate magnetization. On the other hand, the ME effect originates from the change of the electronic band structure by the electric field, while the electron distribution is assumed to stay in equilibrium. Thus the ME effect is mainly considered in insulators, but can also exist in metals^{36,37}. In accordance with these differences in mechanisms between the KME and the ME effects, their symmetry requirements are different. In the ME effect, inversion and time-reversal symmetries should be broken. On the other hand, in the Edelstein effect, the inversion symmetry should be broken, but the time-reversal symmetry can either be preserved or broken. It is seen in chiral systems^{1–3,10,11,13,14}, and in polar systems¹⁵.

Magnetoelectric tensors may require careful consideration of boundaries. While orbital magnetization is independent of the boundary^{38–43}, the orbital magnetization when an electric field is applied may not have such properties. The general orbital magnetoelectric response^{32–35} depends on the boundary⁴¹. Therefore, it is important to study the effect of the boundary of the response of orbital magnetization.

In this paper, we investigate KME in topological insulators such as three-dimensional Chern insulators and Z_2 topological insulators (Z_2 -TIs)^{44–46} in which the currents are localized on the surface. First, we calculate the KME in three-dimensional topological insulators with the chiral crystal structures. Second, we derive the KME based on the surface Hamiltonian, and we show that this effect depends on surface states. Finally, we propose candidate materials for this effect and estimate the values of the KME. By comparing the results with the results in a chiral semiconductor tellurium⁵, we show that in topological insulators the orbital magnetization as a response to the current is much larger than metals by many orders of magnitude.

Results

Formulation for KME. We consider a crystal in a shape of a cylinder along the z -axis and calculate its orbital magnetization along the z -axis generated by the current along the z -axis. Let c be the lattice constant along the z -axis. We introduce the velocity operator \mathbf{v} as $\mathbf{v} = -\frac{i}{\hbar}[\mathbf{r}, H]$, where \mathbf{r} is the position operator and H is the Hamiltonian. In the limit of the system length along the z -axis to be infinity, the orbital magnetization at zero temperature is

$$M_z = \frac{1}{2\pi} \int_{-\pi/c}^{\pi/c} dk_z \frac{1}{S} \sum_n^N f(E_n(k_z)) \times \left(-\frac{e}{2}\right) \int dx dy \psi_{n,k_z}^\dagger(x, y) (\mathbf{r} \times \mathbf{v})_z \psi_{n,k_z}(x, y), \quad (1)$$

where $-e$ is the electron charge, $\psi_{n,k_z}(x, y)$ and E_n is the n th occupied eigenstates and energy eigenvalues of H at the Bloch wave-number k_z , respectively. $f(E)$ is the distribution function at the energy E , S is the cross-section of the crystal along the xy -plane and N is the number of occupied states. We note that the position operator \mathbf{r} is unbounded and problematic if a system is infinite in some directions. Nonetheless, in the present case, the system is infinite only along the z -direction, while $(\mathbf{r} \times \mathbf{v})_z$ does not involve z , which means Eq. (1) is well defined. The unit of the orbital magnetization is [A/m] in the SI unit.

Then, within the Boltzman approximation⁴, the applied electric field E_z changes $f(E)$ from $f^0(E)$ into $f(E) = f^0(E) + \frac{e\tau E_z}{\hbar} \frac{\partial f^0(E)}{\partial k_z}$ in a linear order in E_z , where τ is the relaxation time assumed to be constant and $f^0(E)$ is the Fermi distribution function $f^0(E) = (e^{\beta(E-\mu)} + 1)^{-1}$, $\beta = 1/k_B T$, k_B is the Boltzman constant and μ is the chemical potential. Then the orbital magnetization is generated as

$$M_z^{\text{KME}} = \frac{1}{2\pi} \int_{-\pi/c}^{\pi/c} dk_z \frac{1}{S} \sum_n^N \frac{e\tau E_z}{\hbar} \frac{\partial f^0(E_n(k_z))}{\partial k_z} \times \left(-\frac{e}{2}\right) \int dx dy \psi_{n,k_z}^\dagger(x, y) (\mathbf{r} \times \mathbf{v})_z \psi_{n,k_z}(x, y) \quad (2)$$

This is the KME. In Chern insulators, because the TRS is broken, an orbital magnetization is nonzero in equilibrium, and a current leads to a change in an orbital magnetization due to the KME. On the other hand, in Z_2 -TIs, an orbital magnetization vanishes in equilibrium due to TRS, and the KME leads to the appearance of an orbital magnetization. We note that in addition to the off-equilibrium electron distribution discussed above, the electric field also modifies the electronic states. In Z_2 -TIs, where TRS is preserved, this modulation of the electronic states does not lead to the orbital magnetization in the linear order in E_z , because the TRS is preserved within this order. On the other hand, in topological insulators without TRS, such as Chern insulators, this may also contribute to the orbital magnetization. This mechanism is similar to the conventional ME effect in insulators and has been discussed also in metals^{36,37}.

This calculation method is different from that in the previous study on metals^{1,2,4}, where bulk contribution in a system infinite along x and y directions are calculated.

Model calculation on a Chern insulator. As an example of a topological insulator, we consider an orbital magnetization in a Chern insulator with a chiral crystal structure. For this purpose, we introduce a three-dimensional tight-binding model of a layered Chern insulator, as shown in Fig. 1a, connected via right-handed interlayer chiral hoppings (Fig. 1b). Each layer forms a square lattice within the xy -plane, with a lattice constant a , and they are stacked along the z -axis with a spacing c , as shown in detail in the “Methods” section. The Brillouin zone and the band structure are shown in Fig. 1c–e. We set the Fermi energy in the energy gap.

We calculate KME in a one-dimensional quadrangular prism with xz and yz surfaces shown in Fig. 1f (see “Methods” section), with its results in Fig. 1g,h with the interlayer hopping $t_3 = 0.1t_y$ and $t_3 = 0.001t_y$, respectively, for several values of the system size, L_x and L_y , representing the lengths of the crystal in the x and y directions. Thus, the KME is affected by boundaries and system size, and this size dependence remains even when the system size is much larger than the penetration depth of topological surface states. Therefore, KME cannot be defined as a bulk quantity. In contrast, the orbital magnetization in equilibrium is shown to be a bulk quantity in crystals^{38–40} in 2005, which is nontrivial, because the operator for the orbital magnetization involves the position

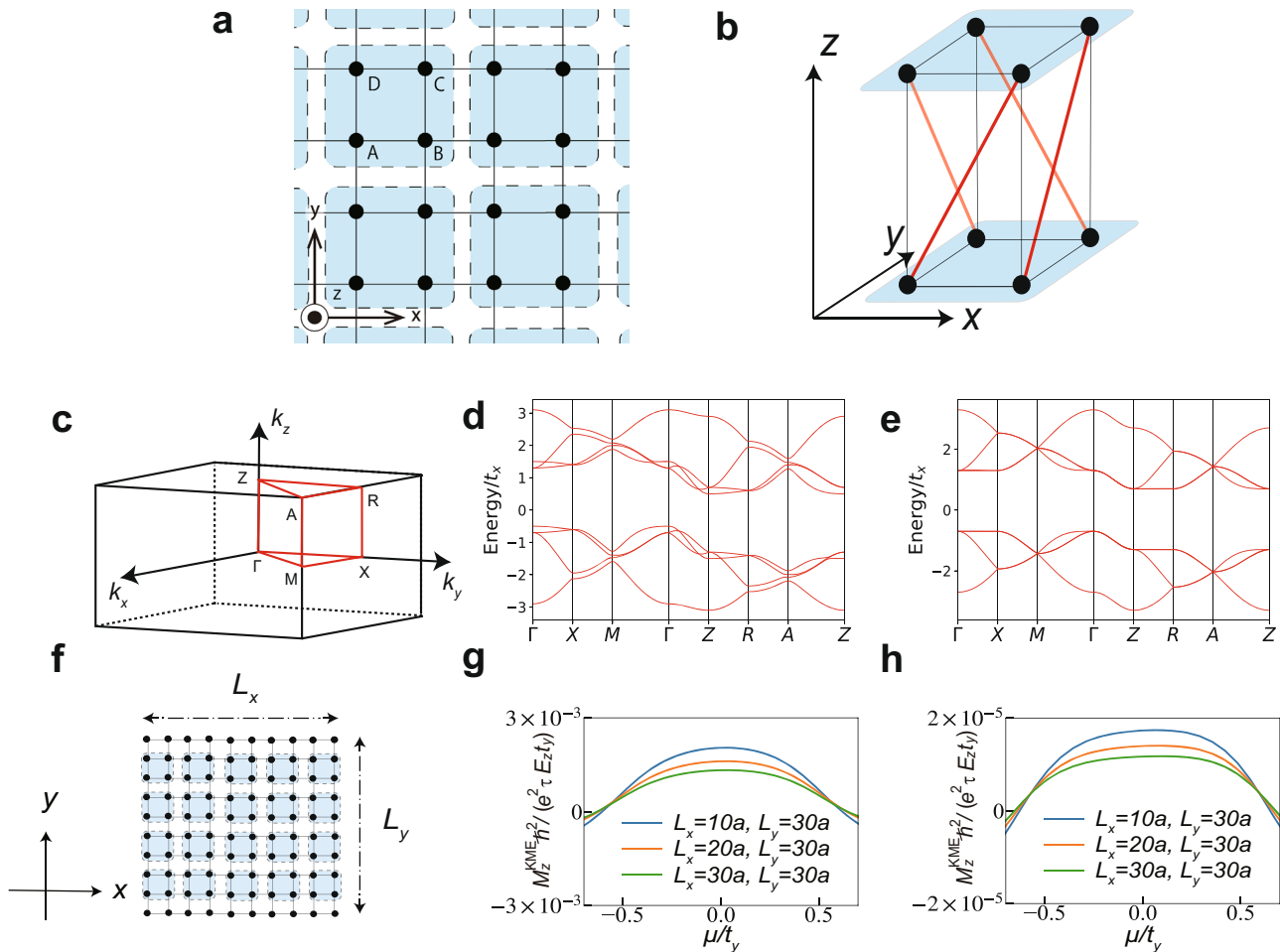


Fig. 1 The model of a Chern insulator with a chiral structure and model calculation of the kinetic magnetoelectric effect (KME). **a** Individual layer of the model forming a square lattice. The blue regions surrounded by the broken line are the unit cells consisting of four sublattices. **b** Schematic picture of the chiral hopping (red) between the two neighboring layers. These hoppings form a structure similar to right-handed solenoids. **c** Brillouin zone of our model with high-symmetry points. **d, e** Energy bands for the Hamiltonian H with parameters (**d**) $t_x = t_y = m = b_x = b_y$, $t_3 = 0.1t_y$ and $t_4 = 0.15t_y$ and (**e**) $t_x = t_y = m = b_x = b_y$, $t_3 = 0.001t_y$ and $t_4 = 0.15t_y$. The symbols such as Γ and X represent high-symmetry points in the wavevector space. **f** A one-dimensional model with periodic boundary conditions in z -direction. It has a rectangle shape of a size $L_x \times L_y$ within the xy plane. The dots are the sites, and the blue squares denote the unit cells, as specified in **a**. In order to see the boundary effect on KME, the outermost layers on the xz surface have no chiral hoppings and those on the yz surface have chiral hoppings. **g, h** KME calculated with parameters (**g**) $t_x = t_y = m = b_x = b_y$, $t_3 = 0.1t_y$ and $t_4 = 0.15t_y$, and (**h**) $t_x = b_x = t_y$, $t_y = b_y = m$, $t_4 = 0.15t_y$, and $t_3 = 0.001t_y$. The blue, orange, and green curves represent the data for $L_x = 10a$, $L_x = 20a$, and $L_x = 30a$, respectively, while L_y is fixed as $L_y = 30a$.

operator \mathbf{r} . Later, we give an interpretation on this characteristic size dependence.

Surface theory of KME for a slab. In topological insulators such as Chern insulators, only the topological surface states can carry a current. Here we calculate the KME using an effective Hamiltonian for the crystal surface. Thereby, we can capture the natures of KME through this surface theory. We consider slab systems, with their surfaces on $y = y_{\pm}$ ($y_+ > y_-$). The slab is sufficiently long along with the x and z directions and we impose periodic boundary conditions in these directions. To induce the orbital magnetization $M_{z,\text{slab}}^{\text{KME}}$, we apply an electric field E_z in the z -direction. Due to the interlayer chiral hoppings, the surface current acquires a nonzero z -component (Fig. 2a).

Let $E_- = E_-(k_x, k_z) (= E_-(k_x, k_z + \frac{\pi}{c}))$ be the surface-state dispersion on the $y = y_-$ surface as shown in Fig. 2b,c. For simplicity, we assume C_{2z} symmetry of the system. Then the surface state dispersion on the $y = y_+$ surface is given by $E_+ = E_+(k_x, k_z) = E_-(-k_x, k_z)$. Here, we assume that the surface

states are sharply localized at $y = y_{\pm}$, namely, we ignore finite-size effects due to a finite penetration depth. Then, we rewrite Eq. (2) to

$$M_{z,\text{slab}}^{\text{KME}} = \frac{e^2 \tau E_z}{2\hbar^2} \int_{-\pi/c}^{\pi/c} \frac{dk_x}{(2\pi)^2} \times \frac{\partial E(k'_x, k_z)}{\partial k_x} \text{sgn} \left(\frac{\partial E(k'_x, k_z)}{\partial k_x} \right) \Big|_{E(k'_x, k_z) = \mu}, \tag{3}$$

(see Supplementary Note 1 for details). We note that the Fermi surface depends on the surface termination, and so does the KME. We also confirm the surface dependence from numerical calculations as shown in Fig. 2d-i. This formula applies to any topological insulators such as Z_2 -TIs⁴⁴⁻⁴⁶ (see Supplementary Note 2).

Surface theory of KME for a cylinder. From this slab calculation, we calculate the KME for a cylinder geometry. We consider a current along the z -direction in a one-dimensional quadrangular prism with xz and yz surfaces (surfaces I-IV in Fig. 3a) through its surface Hamiltonian. Let L_x and L_y denote the system sizes

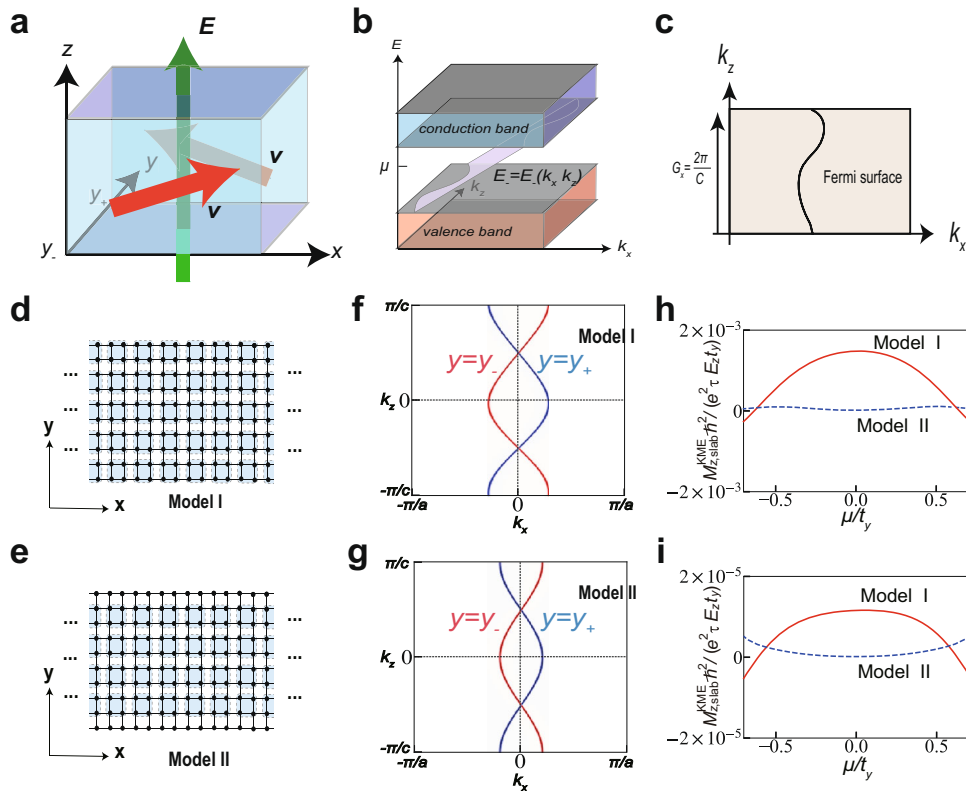


Fig. 2 Chern insulator with a chiral structure and its kinetic magnetoelectric effect (KME) in slab systems. **a** Surface velocities (red arrow) of the topological surface states under an electric field **E** (green arrow). **b, c** Band structure of the topological chiral surface states on the $y = y_-$ surface. Their **(b)** dispersion and **(c)** Fermi surface are shown. In **b**, the valence and conduction bands are represented by orange and blue boxes, and the topological surface states are drawn in purple in between the two bands. **c** is the Fermi surface, which is a section of **b** at the energy E equal to the chemical potential μ . **d** Slab models I and II with chiral hopping on the surface. Only the section along the xy plane is shown. The dots are the sites of the tight-binding model, and the blue boxes represent the unit cells, as shown in Fig. 1a. **e** Slab model II with no chiral hopping on the surface. The symbols are the same as **(d)**. **f, g** The Fermi surfaces for the slab models **(f)** I and **(g)** II with parameters $t_x = t_y = m = b_x = b_y$, $t_3 = 0.1t_y$, $t_4 = 0.15t_y$, and $\mu = 0$. The red and blue curves represent Fermi surfaces on the $y = y_-$ and $y = y_+$ planes, respectively. **h, i** KME for the slab models I and II, shown as red solid lines and as blue broken lines, respectively, with parameters **(h)** $t_x = t_y = m = b_x = b_y$, $t_3 = 0.1t_y$, and $t_4 = 0.15t_y$ and **(i)** $t_x = t_y = m = b_x = b_y$, $t_3 = 0.001t_y$, and $t_4 = 0.15t_y$.

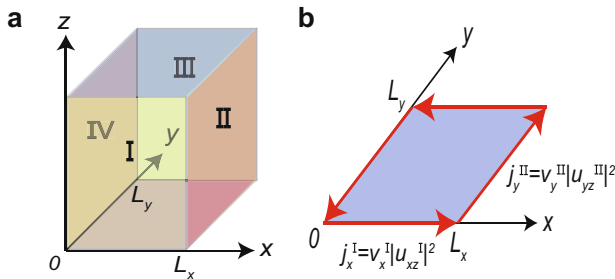


Fig. 3 One-dimensional prism of a Chern insulator. **a** Schematic figure of the one-dimensional prism of a Chern insulator, extended along z -axis, with its size $L_x \times L_y$ within the xy plane. We call the four side surfaces I, II, III and IV. **b** The schematic figure for current conservation at the corners around the one-dimensional prism in **a**. Here, j_x^I and j_y^II are current densities in the circumferential direction of the prism on the surfaces I and II, respectively, and we impose them to be equal. v_x^I and v_y^II are corresponding velocities of electrons, and u_{xz}^I and u_{yz}^II are amplitudes of the wavefunctions in the respective surfaces.

along the x and y directions, respectively. Because the KME is sensitive to differences in crystal surfaces, as shown in-slab systems, we consider the individual surfaces separately.

In particular, in Chern insulators, we can calculate the energy eigenstates for the whole system from that for the surface

Hamiltonians. For simplicity, we assume twofold rotation symmetry C_{2z} of the system, which relates between I and III, and between II and IV. Then, only the surface I and II are independent. We write down the eigenequations for these surfaces as

$$H^I \psi_{k_x k_z}^I(x, z) = E_{k_x k_z}^I \psi_{k_x k_z}^I(x, z), \tag{4}$$

$$H^{II} \psi_{k_y k_z}^{II}(y, z) = E_{k_y k_z}^{II} \psi_{k_y k_z}^{II}(y, z), \tag{5}$$

where H^I and H^{II} are the surface Hamiltonians for the surfaces I and II, respectively, and $\psi_{k_x k_z}^I = u_{k_x k_z}^I(k_x, k_z) e^{ik_x x} e^{ik_z z}$ and $\psi_{k_y k_z}^{II} = u_{k_y k_z}^{II}(k_y, k_z) e^{ik_y y} e^{ik_z z}$ are Bloch eigenstates on the surfaces I and II, respectively. We can determine these eigenstates from four conditions, equality of the energy eigenvalues, current conservation at the corner (Fig. 3b)^{47–49}, periodic boundary condition on the crystal surface, and the normalization condition (see Supplementary Note 3).

Thus we obtain a formula for KME in a one-dimensional prism of a three-dimensional Chern insulator

$$M_z^{\text{KME}} = -\frac{e^2 \tau E_z}{\hbar} \frac{1}{(2\pi)^2} \int_{-\pi/c}^{\pi/c} dk_z \frac{L_x \frac{\partial k_x^I}{\partial k_z} + L_y \frac{\partial k_y^{II}}{\partial k_z}}{\frac{L_x}{v_x^I} + \frac{L_y}{v_y^{II}}} \Big|_{E=\mu}, \tag{6}$$

where $v_x^I = \frac{1}{\hbar} \frac{\partial E^I}{\partial k_x}$ and $v_y^{II} = \frac{1}{\hbar} \frac{\partial E^{II}}{\partial k_y}$ and $k_x^I(k_z, E)$ and $k_y^{II}(k_z, E)$ are functions obtained from $E = E_{k_x k_z}^I$ and $E = E_{k_y k_z}^{II}$, respectively.

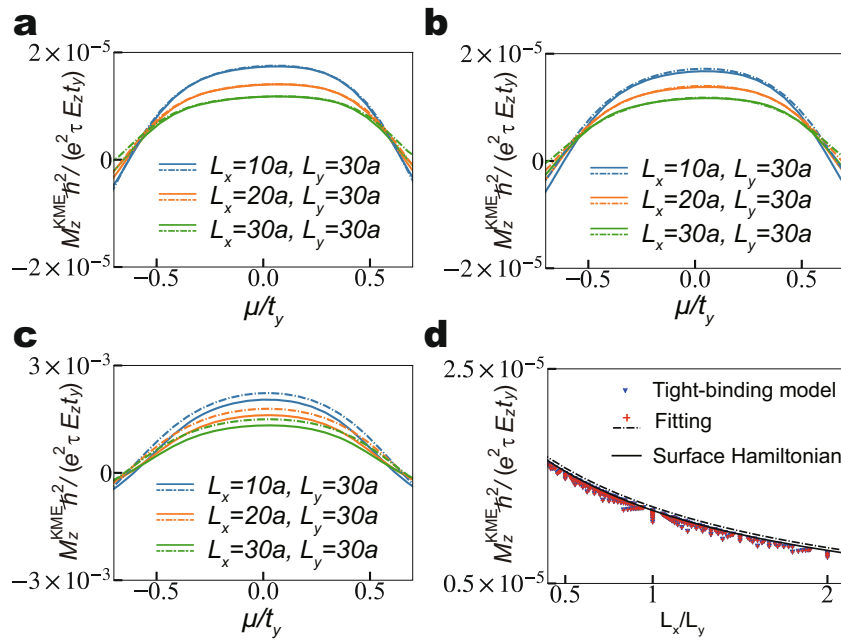


Fig. 4 Kinetic magnetoelectric effect (KME) in one-dimensional systems. **a–c** KME is calculated from two different methods; one is a direct calculation by Eq. (2) (solid lines) and the other is by a combination of calculation results for surfaces along xz and yz planes based on Eq. (7) (dashed lines). Parameter values are **(a)** $t_x = t_y = m = b_x = b_y$, $t_3 = 0.001t_y$ and $t_4 = 0.15t_y$, **(b)** $t_x = b_x = 1.1t_y$, $t_y = b_y = m$, $t_4 = 0.15t_y$ and $t_3 = 0.001t_y$, and **(c)** $t_x = t_y = m = b_x = b_y$, $t_4 = 0.15t_y$ and $t_3 = 0.1t_y$. The results are shown for $L_x = 10a$ (blue), $L_x = 20a$ (orange), and $L_x = 30a$ (green), while L_y is fixed to be $30a$. **d** Dependence of the KME on the aspect ratio within the xy plane with parameters $t_x = b_x = 1.1t_y$, $t_y = b_y = m$, $t_4 = 0.15t_y$, $t_3 = 0.001t_y$, and $\mu = 0$. Blue points represent the result of direct calculation by Eq. (2) for various system sizes. With parameter values $t_x = b_x = 1.1t_y$, $t_y = b_y = m$, $t_4 = 0.15t_y$, $t_3 = 0.001t_y$, and $\mu = 0$, we calculate the KME with various system sizes. The system sizes are $(L_x, L_y) \in \{10a, 12a, \dots, 38a\} \times \{10a, 12a, \dots, 38a\}$. Red points represent the result of fitting the numerical results of Eq. (2) with the fitting function in Eq. (13), and its limit for $L_x, L_y \rightarrow \infty$ is shown as the dashed line. The solid line represents the results of the surface theory in Eq. (7).

When v_x and v_y are almost independent of k_z , we approximate Eq. (6):

$$M_z^{KME} = 2 \frac{\frac{L_x}{\langle v_x^I \rangle} M_{z,slab}^{I,KME} + \frac{L_y}{\langle v_y^{II} \rangle} M_{z,slab}^{II,KME}}{\frac{L_x}{\langle v_x^I \rangle} + \frac{L_y}{\langle v_y^{II} \rangle}}, \quad (7)$$

where $M_{z,slab}^{I,KME}$ and $M_{z,slab}^{II,KME}$ represent the KME for a slab (Eq. (3)) with the surface I and that with the surface II, respectively. Thus, the KME of the one-dimensional system can be well approximated by Eq. (7) expressed in terms of that for the slabs along xz and along yz planes.

In general topological insulators, we can also derive KME in terms of a simple picture of a combined circuit, consisting of four surfaces I–IV with anisotropic transport coefficients. We obtain

$$M_z^{KME} = j_{circ} = \frac{\frac{L_x}{\sigma_{xx}^I} \sigma_{xz}^I + \frac{L_y}{\sigma_{yy}^{II}} \sigma_{yz}^{II}}{\frac{L_x}{\sigma_{xx}^I} + \frac{L_y}{\sigma_{yy}^{II}}} E_z, \quad (8)$$

where j_{circ} is the circulating current density within the xy plane around the prism per unit length along the z -direction. $\sigma_{ij}^{I,II}$ is the electric conductivity tensor for the surfaces I and II (see Supplementary Note 4). On the other hand, we can also show $M_{z,slab}^{I,KME} = \frac{1}{2} \sigma_{xz}^I E_z$, $M_{z,slab}^{II,KME} = \frac{1}{2} \sigma_{yz}^{II} E_z$. In Chern insulators, by using $\sigma_{xx}^I \propto \langle v_x \rangle$ and $\sigma_{yy}^{II} \propto \langle v_y \rangle$, we arrive at Eq. (7). Thus, we can calculate the KME from the surface electrical conductivity from Eq. (8), which depends on the aspect ratio L_x/L_y .

We numerically confirm that the results of direct calculation by Eq. (2) and those for surface calculation by Eq. (7) agree well (Fig. 4a–c). When the interlayer hopping is large (Fig. 4c), they

slightly deviate from each other. This is because we cannot ignore the k_z dependence of v_x and v_y , and they are out of the scope of the approximate expression (Eq. 7).

Finite-size effect. In our approximation theory, we assumed that the surface current is localized at the outermost sites and ignored a finite penetration depth. In fact, we can fit well the data with various system sizes with a trial fitting function which includes a finite-size effect in Eq. (7) (see “Methods” section and Supplementary Note 5). From these results, the finite-size effect is of the order $1/L$ in the leading order, coming from the finite penetration depth. When the system size is much larger than the penetration depth, the result is well described by the surface theory as shown in Fig. 4d.

Materials. Topological insulators without inversion symmetry can be a good platform for obtaining large KME because the current flows on the surface. Therefore, the closed-loop created by the current is macroscopic and it efficiently induces orbital magnetization. In contrast, in the conventional KME in metals, a bulk current generates microscopic current loops in the bulk, which leads to a much smaller effect than a surface current in topological insulators. One can also regard this set of current loops as a macroscopic current loop along the surface, but the current, in this case, is of a microscopic amount, determined by the current per bulk unit cell. Therefore, the resulting effect in bulk metals is much smaller than the KME in topological insulators, where the current along the surface is of macroscopic size. Moreover, the surface states of topological materials are robust against perturbations caused by impurities.

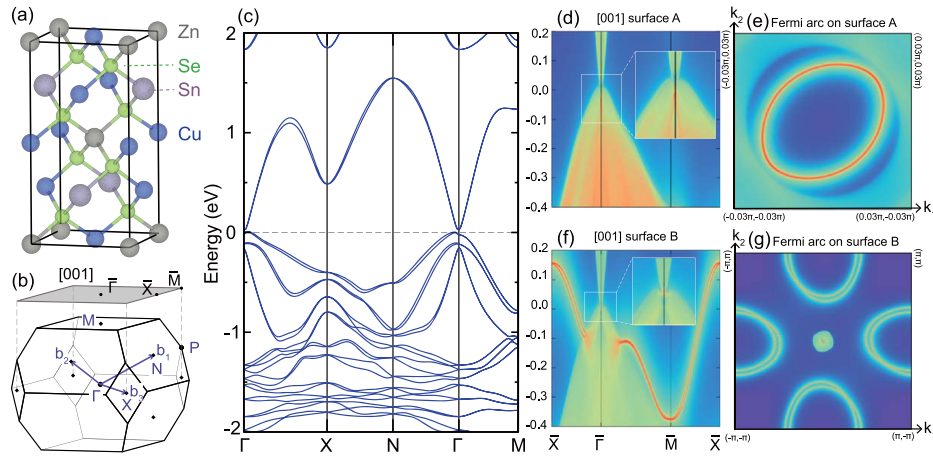


Fig. 5 First-principle calculations on $\text{Cu}_2\text{ZnSnSe}_4$. **a** Crystal structure of $\text{Cu}_2\text{ZnSnSe}_4$. **b** Brillouin zone and surface Brillouin zone along [001] direction. **c** Electronic structure with spin-orbit coupling for the bulk. **d–e** Surface states and Fermi arcs calculation on the [001] surface with Cu-Sn layer termination (surface A). **f–g** Surface states and Fermi arcs calculation on the [001] surface with Se layer termination (surface B).

Under the non-inversion-symmetry constraint, we cannot diagnose Z_2 -TIs easily because the Z_2 topological invariant is expressed in terms of k -space integrals. Our idea here is to use S_4 symmetry to diagnose Z_2 -TIs, where we only need to calculate wavefunctions at four momenta according to the symmetry-based indicator theories^{50–52}. After searching in the topological material database⁵³, we notice that $\text{Cu}_2\text{ZnSnSe}_4$ ⁵⁴ with **82** and CdGeAs_2 with **122** are two ideal candidates of Z_2 -TIs with a direct gap for obtaining a large KME (see Supplementary Note 6 for details). In the following, we will use $\text{Cu}_2\text{ZnSnSe}_4$, which only has S_4 symmetry as shown in Fig. 5a, as an example to show the magnitude of the KME with different surfaces and different surfaces terminations.

Since the magnetoelectric tensor for the space group **82**, defined by $\mathbf{M} = \boldsymbol{\alpha}\mathbf{E}$, is $\alpha_{82} = \begin{bmatrix} \alpha_{11} & \alpha_{12} & 0 \\ \alpha_{12} & -\alpha_{11} & 0 \\ 0 & 0 & 0 \end{bmatrix}$, we can obtain an orbital

magnetization M_1^{KME} by adding an external electric field E_1 , through the surface currents both on the [001] surface and on the [010] surface thanks to the nonzero α_{11} (see Supplementary Note 7 for details). In our discussion of the KME effect, we set the current direction to be along z -axis. Therefore we will set the 1-axis in the above magnetoelectric tensor to be the z -axis in our theory.

Figure 5b, c is the Brillouin zone and the band structure of $\text{Cu}_2\text{ZnSnSe}_4$ with a gap, through the first-principle calculations whose details are explained in “Methods” section. On the [001] surface, terminations with Cu-Sn layer (surface A) and with Se layer (surface B) have different surface energies and Fermi surfaces, as shown in Fig. 5d–g, which contribute to a magnetoelectric susceptibility of $\alpha_{11}^{\text{A}} = -1.804 \times 10^8 \text{s}^{-1} \Omega^{-1} \cdot \tau$ and $\alpha_{11}^{\text{B}} = -2.565 \times 10^9 \text{s}^{-1} \Omega^{-1} \cdot \tau$, respectively. On the A surface, there is a single surface Dirac cone at Γ point, forming an electron-like Fermi surface. On the B surface, the Dirac cone at Γ point forms an almost zero Fermi surface, but two surface Dirac cones at two \bar{X} momenta form two hole-like Fermi surfaces. Because the Fermi surfaces on the B surface are much larger than those on the A surface, the magnetoelectric susceptibility on the B surface is one order of magnitude larger than that on the A surface. Similar calculations on the [010] surface area in Supplementary Note 8, and the result is $\alpha_{11}^{\text{C}} = -2.324 \times 10^9 \text{s}^{-1} \Omega^{-1} \cdot \tau$ for surface C.

Let us compare the results with metallic materials in the bulk. For simplicity, we focus on the cases with the electric field \mathbf{E} and

the resulting magnetization \mathbf{M}^{KME} along the z -direction. This kinetic magnetoelectric response is expressed as $M_z^{\text{KME}} = \alpha_{zz} E_z$, and the conductivity is $j_z = \sigma_{zz} E_z$. Thus the magnetization in response to the current is $M_z^{\text{KME}} = (\alpha_{zz} / \sigma_{zz}) j_z$. In the relaxation time approximation, both α_{zz} and σ_{zz} are proportional to the relaxation time τ . For simplicity we consider the system to be a cube with its size $L \times L \times L$. In the bulk metallic systems, the current is carried by the bulk states, and $\alpha_{zz} \propto L^0$, $\sigma_{zz} \propto L^0$. On the other hand, in topological systems, only the surface conducts the current, and the conductivity σ_{zz} scales as $\sigma_{zz} \propto L^{-1}$. On the other hand, we have shown $\alpha_{zz} \propto L^0$, which means that α_{zz} is an intensive quantity. Thus, in topological insulators, the scaling of the KME as a response to the electric field is represented by the response coefficient $\alpha_{zz} \propto L^0$. Meanwhile, the response coefficient $\alpha_{zz} / \sigma_{zz}$ to the current is proportional to L . It means that as a response to the current, topological materials will generate a large amount of orbital magnetization as compared to metals.

We compare our results with KME in p -doped tellurium, which has a chiral crystal structure⁵. For the acceptor concentration $N_a = 4 \cdot 10^{14} \text{cm}^{-3}$ at 50 K, the induced orbital magnetizations is $M_z^{\text{KME}} = 7.0 \cdot 10^{-8} \mu_B / \text{atom} \sim 1.85 \times 10^{-2} \text{A/m}$ by a current density $j_z = 1000 \text{A/cm}^2$. Thus the response coefficient of the orbital magnetization M_z^{KME} to the current density j_z is $\alpha_{zz} / \sigma_{zz} = 1.85 \times 10^{-9} \text{m}$. If we approximate σ_{zz} by $\sigma_{zz} \sim \frac{N_a e^2 \tau}{m}$ with the electronic charge e and mass m , we get $\alpha = 2.1 \times 10^4 \text{s}^{-1} \Omega^{-1} \cdot \tau$. For other acceptor concentrations $N_a = 4 \cdot 10^{16} \text{cm}^{-3}$ and $N_a = 1 \cdot 10^{18} \text{cm}^{-3}$, one can similarly get $\alpha_{zz} = 2.1 \times 10^6 \text{s}^{-1} \Omega^{-1} \cdot \tau$ and $\alpha_{zz} = 2.3 \times 10^7 \text{s}^{-1} \Omega^{-1} \cdot \tau$. Thus, the size of α_{zz} for the topological insulator $\text{Cu}_2\text{ZnSnSe}_4$ is larger than that of Te by two to five orders of magnitude.

On the other hand, in topological insulators, the induced orbital magnetization as a response to the current becomes huge compared with metals. To show this, we consider a system with surfaces having anisotropic transport coefficients with sheet resistance $\sigma_{xz, \square}$ and $\sigma_{zz, \square}$, where \square denotes a sheet conductance. Then we can define an angle θ by $\sigma_{xz, \square} / \sigma_{zz, \square} = \tan \theta$, where θ describes an angle between the electric field along the z -direction and the surface current density \mathbf{j}^{surf} . For example, for the [001] surface of $\text{Cu}_2\text{ZnSnSe}_4$, we get $\sigma_{21, \square}^{\text{A}} = 2\alpha_{11}^{\text{A}} = -3.6 \times 10^8 \text{s}^{-1} \Omega^{-1} \cdot \tau$, $\sigma_{11, \square}^{\text{A}} = 7.3 \times 10^8 \text{s}^{-1} \Omega^{-1} \cdot \tau$, $\sigma_{21, \square}^{\text{B}} = 2\alpha_{11}^{\text{B}} = -5.1 \times 10^9 \text{s}^{-1} \Omega^{-1} \cdot \tau$, $\sigma_{11, \square}^{\text{B}} = 2.0 \times 10^{10} \text{s}^{-1} \Omega^{-1} \cdot \tau$, which yield $\tan \theta^{\text{A}} = -0.49$ and $\tan \theta^{\text{B}} = -0.26$ by identifying $x=2$ and $z=1$. Then the total

current along the z direction is $4Lj_z$ while the circulating current is $j_{\text{circ}} = j_x^{\text{surf}} = j_z^{\text{surf}} \tan \theta$. Thus the magnetization response M_z^{KME} to the current density $j_z (= 4Lj_z^{\text{surf}}/L^2)$ is $M_z^{\text{KME}}/j_z = (j_{\text{circ}}/j_z^{\text{surf}})(L/4) = (L/4) \tan \theta$, which is proportional to the system size. It is the response coefficient α/σ shown in Table 1. Thus for the macroscopic system size, the response M_z^{KME}/j_z is also of the macroscopic size such as millimeters, and it is much order of magnitude larger than that in tellurium, where M_z^{KME}/j_z is evaluated to be $M_z^{\text{KME}}/j_z = 1.85 \times 10^{-9} \text{m}$.

This scaling to the system size shows a prominent difference in the KME in topological insulators from similar effects. In bulk metals studied in previous works, the KME is always independent of the system size L . In topological insulators, the current induces both the spin and the orbital magnetizations, and we propose that only the orbital magnetization shows a different scaling behavior. As a comparison, we calculate the spin magnetization induced by the electric field in $\text{Cu}_2\text{ZnSnSe}_4$, with calculation details and spin textures presented in Supplementary Note 9, and obtain $\alpha_{11}^{\text{A,spin}} = 2.798 \times 10^{-2} \text{m} \cdot \text{s}^{-1} \Omega^{-1} \cdot \tau/L_y$, and $\alpha_{11}^{\text{B,spin}} = -2.575 \text{m} \cdot \text{s}^{-1} \Omega^{-1} \cdot \tau/L_y$. Thus it inversely scales with the system size along the y -direction. Thus suppose the system size of 1mm, they are of the order $10^1 - 10^3 \text{s}^{-1} \Omega^{-1} \cdot \tau$, and the orbital magnetization from the KME, having $10^8 - 10^9 \text{s}^{-1} \Omega^{-1} \cdot \tau$, is larger than the spin counterpart by 5–8 orders of magnitude. Thus, while the spin and orbital magnetization behave similarly in bulk metals, they are quite different in topological insulators, which is the main point of the present paper.

Conclusion

In summary, we propose KME in topological insulators with chiral structures. This KME is carried by the surface current due to the asymmetric crystal structure of the surface. Therefore, the KME is sensitive to surface terminations, and it cannot be defined as a bulk quantity. We derive a formula for the KME as a surface quantity using the surface Hamiltonian and show that it fits with numerical results.

In theoretical treatments, atomic orbitals can classify the orbital magnetization into intraatom and interatom contributions. Some atomic orbitals such as $p_x \pm ip_y$ have orbital angular momentum, which leads to corresponding intraatomic orbital magnetization. On the other hand, the hopping between atoms leads, to interatomic orbital magnetization. In tight-binding models with atomic orbitals, they are separately calculated. In some papers^{10,11}, the intraatomic orbital magnetization is studied, while the interatomic one is studied in other papers^{1,2,15}. In real materials, these two contributions are not separable, and in the ab initio calculation⁵, their sum is calculated. In this paper, we found that in topological materials, the interatomic contribution is much larger due to the macroscopic current loop. We show that the response to the current in topological insulators is much larger than in metals. In Table 1, we show scaling behaviors of the spin and intraatom/interatom orbital magnetizations for metals and TIs. The KME is shown as responses to an electric field, α , and to a current, α/σ . In particular, in the response to a current, α/σ , it scales as L^1 only in the interatom orbital magnetization, while other entities scale with L^0 . This shows a particular feature of the interatom orbital magnetization generated by a current proposed in the present paper.

In this paper, we put two Z_2 TIs as candidates for the topological KME. In addition to Chern insulators and Z_2 TIs, other classes of topological insulators such as various classes of topological crystalline insulators, and topological semimetals will also show the topological KME. In topological semimetals, topological

Table 1 Scaling behaviors of interatom and intraatom orbital and spin magnetizations versus the system size L , as a response to the electric field represented by α , and to the current α/σ in metals and in topological insulators (TIs).

		σ	α	α/σ
Interatom orbital	Metal	L^0	L^0	L^0
	TI	L^{-1}	L^0	L^1
Intraatom orbital	Metal	L^0	L^0	L^0
	TI	L^{-1}	L^{-1}	L^0
Spin	Metal	L^0	L^0	L^0
	TI	L^{-1}	L^{-1}	L^0

The scaling of the conductivity σ is also shown.

surface states coexist with bulk metallic states, but the contribution from the former overwhelms that from the latter, and the topological KME is expected.

Methods

Details of the first-principle calculations. First-principle calculations of $\text{Cu}_2\text{ZnSnSe}_4$ are implemented in the Vienna ab initio simulation package (VASP)^{55–57} with Perdew-Burke-Ernzerhof exchange-correlation. A Γ -centered Monkhorst-Pack grid with $10 \times 10 \times 10$ k -points and 460.8 eV for the cut-off energy of the plane wave basis set is used for the self-consistent calculation. Surface states and Fermi surfaces calculations are performed by the tight-binding model obtained by the maximally localized Wannier functions⁵⁸.

Details of the model Hamiltonian. We consider a Chern insulating system with a chiral crystal structure. The model is composed of infinite layers of the two-dimensional Wilson-Dirac model^{59,60}. The lattice sites are expressed by (i, j, l) , with i, j, l being integers, specifying the x, y , and z -coordinates. At each lattice site, we consider two orbitals 1 and 2. Let $c_{i,j,l,\sigma}$ denote the annihilation operator of electrons at the (i, j, l) -site with orbital $\sigma = (1, 2)$, and we write $c_{i,j,l} = (c_{i,j,l,1}, c_{i,j,l,2})^T$. The model Hamiltonian is $H = H_{\text{WD}}(m, t_x, t_y, b_x, b_y) + H_{\text{interlayer}}(t_3, t_4)$, where H_{WD} is an in-plane Wilson-Dirac Hamiltonian, and $H_{\text{interlayer}}$ is an interlayer Hamiltonian representing a structure similar to right-handed solenoids. The in-plane Wilson-Dirac Hamiltonian is

$$\begin{aligned}
 H_{\text{WD}} = & m \sum_{i,j,l} c_{i,j,l}^\dagger \sigma_z c_{i,j,l} \\
 & - \frac{it_x}{2} \sum_{i,j,l} (c_{i,j,l}^\dagger \sigma_x c_{i+1,j,l} - \text{H.c.}) \\
 & - \frac{it_y}{2} \sum_{i,j,l} (c_{i,j,l}^\dagger \sigma_y c_{i,j+1,l} - \text{H.c.}) \\
 & + \frac{b_x}{2} \sum_{i,j,l} (c_{i,j,l}^\dagger \sigma_z c_{i+1,j,l} + \text{H.c.} - 2c_{i,j,l}^\dagger \sigma_z c_{i,j,l}) \\
 & + \frac{b_y}{2} \sum_{i,j,l} (c_{i,j,l}^\dagger \sigma_z c_{i,j+1,l} + \text{H.c.} - 2c_{i,j,l}^\dagger \sigma_z c_{i,j,l}),
 \end{aligned} \quad (9)$$

where H.c. stands for Hermitian conjugate of the preceding terms, \dagger represents Hermitian conjugate, and m, t_x, t_y, b_x , and b_y are real parameters. This Hamiltonian H_{WD} can be rewritten in the momentum space as

$$\begin{aligned}
 \tilde{H}_{\text{WD}}(\mathbf{k}) = & t_x \sin k_x a \sigma_x + t_y \sin k_y a \sigma_y \\
 & + (m - b_x(1 - \cos k_x a) - b_y(1 - \cos k_y a)) \sigma_z,
 \end{aligned} \quad (10)$$

where \mathbf{k} is the Bloch wavenumber. An isotropic version of the two-dimensional Wilson-Dirac model with $b \equiv b_x = b_y$ and $t_x = t_y$ exhibits the Chern insulating phase when $0 < m/b < 2$ and $2 < m/b < 4$ ⁶⁰. Next, we add interlayer hoppings, including a direct hopping t_4 along the z -axis and a chiral hopping t_3 , where t_3 and t_4 are real parameters. To describe the chiral hopping t_3 , the lattice sites in the square lattice in each layer into groups of four sites, $(2i-1, 2j-1)$, $(2i-1, 2j)$, $(2i, 2j-1)$, and $(2i, 2j)$ where i and j are integers, and we introduce chiral hoppings between the groups on the neighboring layers. Then the total Hamiltonian for this model on a tetragonal lattice is given by

$$H = H_{\text{WD}} + H_{\text{interlayer}}, \quad (11)$$

where

$$\begin{aligned}
 H_{\text{interlayer}} = & t_3 \sum_{i,j,l} (c_{2i-1,2j-1,l}^\dagger c_{2i,2j-1,l+1} + H.c.) \\
 & + t_3 \sum_{i,j,l} (c_{2i,2j-1,l}^\dagger c_{2i,2j,l+1} + H.c.) \\
 & + t_3 \sum_{i,j,l} (c_{2i,2j,l}^\dagger c_{2i-1,2j,l+1} + H.c.) \\
 & + t_3 \sum_{i,j,l} (c_{2i-1,2j,l}^\dagger c_{2i-1,2j-1,l+1} + H.c.) \\
 & + t_4 \sum_{i,j,l} (c_{i,j,l}^\dagger c_{i,j,l+1} + H.c.).
 \end{aligned} \quad (12)$$

These hoppings in $H_{\text{interlayer}}$ form structures similar to right-handed solenoids. When H_{WD} is in the Chern insulator phase, even if H_{WD} is perturbed by $H_{\text{interlayer}}$, the system remains in the Chern insulator with the Chern number within the xy plane equal to -1 as long as t_3 and t_4 are small. In the main text, we are interested in the KME due to the topological surface states in the topological Chern insulating phase, in which the Fermi energy is in the energy gap.

Fitting function for KME. By taking into account the finite-size effect in Eq. (7), we give a fitting function. The finite penetration depth of the surface states will lead to $O(1/L)$ correction to the KME, and that around the corner will lead to $O(1/L^2)$ correction³⁸. Thus, the fitting function is

$$M_z^{\text{KME}} = \frac{w_1 L_x + w_2 L_y + w_3 + \frac{w_4}{L_x} + \frac{w_5}{L_y}}{w_6 L_x + w_7 L_y}, \quad (13)$$

where $w_i (i = 1, 2, \dots, 7)$ are real constants.

Data availability

The datasets generated during and/or analyzed during this study are available from the corresponding authors on reasonable request.

Code availability

The source code for the calculations performed in this work is available from the corresponding authors upon reasonable request.

Received: 18 January 2021; Accepted: 2 August 2021;

Published online: 21 September 2021

References

- Yoda, T., Yokoyama, T. & Murakami, S. Current-induced orbital and spin magnetizations in crystals with helical structure. *Sci. Rep.* **5**, 12024 (2015).
- Yoda, T., Yokoyama, T. & Murakami, S. Orbital Edelstein effect as a condensed-matter analog of solenoids. *Nano Lett.* **18**, 916–920 (2018).
- Furukawa, T., Shimokawa, Y., Kobayashi, K. & Ito, T. Observation of current-induced bulk magnetization in elemental tellurium. *Nat. Commun.* **8**, 954 (2017).
- Zhong, S., Moore, J. E. & Souza, I. Gyrotropic magnetic effect and the magnetic moment on the fermi surface. *Phys. Rev. Lett.* **116**, 077201 (2016).
- Tsirkin, S. S., Puentes, P. A. & Souza, I. Gyrotropic effects in trigonal tellurium studied from first principles. *Phys. Rev. B* **97**, 035158 (2018).
- Wang, Y.-Q., Morimoto, T. & Moore, J. E. Optical rotation in thin chiral/twisted materials and the gyrotropic magnetic effect. *Phys. Rev. B* **101**, 174419 (2020).
- Moore, J. E. & Orenstein, J. Confinement-induced Berry phase and helicity-dependent photocurrents. *Phys. Rev. Lett.* **105**, 026805 (2010).
- Sodemann, I. & Fu, L. Quantum nonlinear Hall effect induced by Berry curvature dipole in time-reversal invariant materials. *Phys. Rev. Lett.* **115**, 216806 (2015).
- Ma, Q. et al. Observation of the nonlinear Hall effect under time-reversal-symmetric conditions. *Nature* **565**, 337–342 (2018).
- Shalygin, V. A., Sofronov, A. N., Vorob'ev, L. E. & Farbshtein, I. I. Current-induced spin polarization of holes in tellurium. *Phys. Solid State* **54**, 2362–2373 (2012).
- Koretsune, T., Arita, R. & Aoki, H. Magneto-orbital effect without spin-orbit interactions in a noncentrosymmetric zeolite-templated carbon structure. *Phys. Rev. B* **86**, 125207 (2012).
- Furukawa, T., Watanabe, Y., Ogasawara, N., Kobayashi, K. & Ito, T. Current-induced magnetization caused by crystal chirality in nonmagnetic elemental tellurium. *Phys. Rev. Res.* **3**, 023111 (2021).
- Rou, J., Şahin, C., Ma, J. & Pesin, D. A. Kinetic orbital moments and nonlocal transport in disordered metals with nontrivial band geometry. *Phys. Rev. B* **96**, 035120 (2017).
- Şahin, C., Rou, J., Ma, J. & Pesin, D. A. Pancharatnam-Berry phase and kinetic magnetoelectric effect in trigonal tellurium. *Phys. Rev. B* **97**, 205206 (2018).
- Hara, D., Bahramy, M. S. & Murakami, S. Current-induced orbital magnetization in systems without inversion symmetry. *Phys. Rev. B* **102**, 184404 (2020).
- He, W.-Y., Goldhaber-Gordon, D. & Law, K. T. Giant orbital magnetoelectric effect and current-induced magnetization switching in twisted bilayer graphene. *Nat. Commun.* **11**, 1650 (2020).
- Ma, J. & Pesin, D. A. Chiral magnetic effect and natural optical activity in metals with or without Weyl points. *Phys. Rev. B* **92**, 235205 (2015).
- Massarelli, G., Wu, B. & Paramekanti, A. Orbital edelstein effect from density-wave order. *Phys. Rev. B* **100**, 075136 (2019).
- Edelstein, V. Spin polarization of conduction electrons induced by electric current in two-dimensional asymmetric electron systems. *Solid State Commun.* **73**, 233–235 (1990).
- Ivchenko, E. L. & Pikus, G. E. New photogalvanic effect in gyrotropic crystals. *ZhETF Pisma Redaktsiiu* **27**, 640 (1978).
- Levitov, L. S., Nazarov, Y. V. & Eliashberg, G. M. Magnetoelectric effects in conductors with mirror isomer symmetry. *Sov. Phys. JETP* **61**, 133 (1985).
- Naaman, R. & Waldeck, D. H. Chiral-induced spin selectivity effect. *J. Phys. Chem. Lett.* **3**, 2178–2187 (2012).
- Gohler, B. et al. Spin selectivity in electron transmission through self-assembled monolayers of double-stranded DNA. *Science* **331**, 894–897 (2011).
- Kettner, M. et al. Chirality-dependent electron spin filtering by molecular monolayers of helicenes. *J. Phys. Chem. Lett.* **9**, 2025–2030 (2018).
- Bloom, B. P., Kiran, V., Varade, V., Naaman, R. & Waldeck, D. H. Spin selective charge transport through cysteine capped CdSe quantum dots. *Nano Lett.* **16**, 4583–4589 (2016).
- Dor, O. B., Morali, N., Yochelis, S., Baczewski, L. T. & Paltiel, Y. Local light-induced magnetization using nanodots and chiral molecules. *Nano Lett.* **14**, 6042–6049 (2014).
- Kimura, T. et al. Magnetic control of ferroelectric polarization. *Nature* **426**, 55–58 (2003).
- Katsura, H., Nagaosa, N. & Balatsky, A. V. Spin current and magnetoelectric effect in noncollinear magnets. *Phys. Rev. Lett.* **95**, 057205 (2005).
- Fiebig, M. Revival of the magnetoelectric effect. *J. Phys. D* **38**, R123–R152 (2005).
- Spaldin, N. A. & Fiebig, M. The renaissance of magnetoelectric multiferroics. *Science* **309**, 391–392 (2005).
- Wilczek, F. Two applications of axion electrodynamics. *Phys. Rev. Lett.* **58**, 1799–1802 (1987).
- Essin, A. M., Moore, J. E. & Vanderbilt, D. Magnetoelectric polarizability and axion electrodynamics in crystalline insulators. *Phys. Rev. Lett.* **102**, 146805 (2009).
- Essin, A. M., Turner, A. M., Moore, J. E. & Vanderbilt, D. Orbital magnetoelectric coupling in band insulators. *Phys. Rev. B* **81**, 205104 (2010).
- Malashevich, A., Souza, I., Coh, S. & Vanderbilt, D. Theory of orbital magnetoelectric response. *New J. Phys.* **12**, 053032 (2010).
- Coh, S., Vanderbilt, D., Malashevich, A. & Souza, I. Chern-simons orbital magnetoelectric coupling in generic insulators. *Phys. Rev. B* **83**, 085108 (2011).
- Winkler, R. & Zülicke, U. Collinear orbital antiferromagnetic order and magnetoelectricity in quasi-two-dimensional itinerant-electron paramagnets, ferromagnets, and antiferromagnets. *Phys. Rev. Res.* **2**, 043060 (2020).
- Xiao, C., Liu, H., Zhao, J., Yang, S. A. & Niu, Q. Thermoelectric generation of orbital magnetization in metals. *Phys. Rev. B* **103**, 045401 (2021).
- Ceresoli, D., Thonhauser, T., Vanderbilt, D. & Resta, R. Orbital magnetization in crystalline solids: Multi-band insulators, Chern insulators, and metals. *Phys. Rev. B* **74**, 024408 (2006).
- Thonhauser, T., Ceresoli, D., Vanderbilt, D. & Resta, R. Orbital magnetization in periodic insulators. *Phys. Rev. Lett.* **95**, 137205 (2005).
- Xiao, D., Shi, J. & Niu, Q. Berry phase correction to electron density of states in solids. *Phys. Rev. Lett.* **95**, 137204 (2005).
- Chen, K.-T. & Lee, P. A. Effect of the boundary on thermodynamic quantities such as magnetization. *Phys. Rev. B* **86**, 195111 (2012).
- Bianco, R. & Resta, R. Orbital magnetization as a local property. *Phys. Rev. Lett.* **110**, 087202 (2013).
- Marrazzo, A. & Resta, R. Irrelevance of the boundary on the magnetization of metals. *Phys. Rev. Lett.* **116**, 137201 (2016).
- Fu, L., Kane, C. L. & Mele, E. J. Topological insulators in three dimensions. *Phys. Rev. Lett.* **98**, 106803 (2007).
- Moore, J. E. & Balents, L. Topological invariants of time-reversal-invariant band structures. *Phys. Rev. B* **75**, 121306(R) (2007).
- Hsieh, D. et al. A topological Dirac insulator in a quantum spin Hall phase. *Nature* **452**, 970–974 (2008).
- Raoux, A. et al. Velocity-modulation control of electron-wave propagation in graphene. *Phys. Rev. B* **81**, 073407 (2010).
- Concha, A. & Tešanović, Z. Effect of a velocity barrier on the ballistic transport of Dirac fermions. *Phys. Rev. B* **82**, 033413 (2010).

49. Takahashi, R. & Murakami, S. Gapless interface states between topological insulators with opposite Dirac velocities. *Phys. Rev. Lett.* **107**, 166805 (2011).
50. Po, H. C., Vishwanath, A. & Watanabe, H. Symmetry-based indicators of band topology in the 230 space groups. *Nat. Commun.* **8**, 1–9 (2017).
51. Song, Z., Zhang, T., Fang, Z. & Fang, C. Quantitative mappings between symmetry and topology in solids. *Nat. Commun.* **9**, 1–7 (2018).
52. Khalaf, E., Po, H. C., Vishwanath, A. & Watanabe, H. Symmetry indicators and anomalous surface states of topological crystalline insulators. *Phys. Rev. X* **8**, 031070 (2018).
53. Zhang, T. et al. Catalogue of topological electronic materials. *Nature* **566**, 475–479 (2019).
54. Guen, L., Glaunsinger, W. S. & Wold, A. Physical properties of the quarternary chalcogenides $\text{Cu}_2\text{B}^{\text{II}}\text{C}^{\text{IV}}\text{X}_4$ ($\text{B}^{\text{II}} = \text{Zn, Mn, Fe, Co}$; $\text{C}^{\text{IV}} = \text{Si, Ge, Sn}$; $\text{X} = \text{S, Se}$). *Mater. Res. Bull.* **14**, 463–467 (1979).
55. Kresse, G. & Hafner, J. Ab initio molecular dynamics for liquid metals. *Phys. Rev. B* **47**, 558–561 (1993).
56. Kresse, G. & Hafner, J. Ab initio molecular-dynamics simulation of the liquid-metal–amorphous-semiconductor transition in germanium. *Phys. Rev. B* **49**, 14251–14269 (1994).
57. Kresse, G. & Furthmüller, J. Efficiency of ab-initio total energy calculations for metals and semiconductors using a plane-wave basis set. *Comput. Mater. Sci.* **6**, 15 – 50 (1996).
58. Mostofi, A. A. et al. Wannier90: a tool for obtaining maximally-localised Wannier functions. *Comput. Phys. Commun.* **178**, 685–699 (2008).
59. Creutz, M. & Horváth, I. Surface states and chiral symmetry on the lattice. *Phys Rev D* **50**, 2297–2308 (1994).
60. Yoshimura, Y., Imura, K.-I., Fukui, T. & Hatsugai, Y. Characterizing weak topological properties: Berry phase point of view. *Phys. Rev. B* **90**, 155443 (2014).

Acknowledgements

This work was supported by the Japan Society for the Promotion of Science (JSPS) KAKENHI Grants No. JP18H03678, No. JP20H04633, and No. JP21K13865 and by Elements Strategy Initiative to Form Core Research Center (TIES), from MEXT Grant Number JP-MXP0112101001.

Author contributions

All authors contributed to the main contents of this work. K.O. performed the model calculation and formulated the theory for topological systems, through the discussions

with T.Z. and S.M.T.Z. performed the ab initio calculation. S.M. conceived and supervised the project. All authors drafted the manuscript.

Competing interests

The authors declare no competing interests.

Additional information

Supplementary information The online version contains supplementary material available at <https://doi.org/10.1038/s42005-021-00702-4>.

Correspondence and requests for materials should be addressed to Shuichi Murakami.

Peer review information *Communications Physics* thanks the anonymous reviewers for their contribution to the peer review of this work. This article has been peer reviewed as part of Springer Nature's **Guided Open Access** initiative.

Reprints and permission information is available at <http://www.nature.com/reprints>

Publisher's note Springer Nature remains neutral with regard to jurisdictional claims in published maps and institutional affiliations.



Open Access This article is licensed under a Creative Commons Attribution 4.0 International License, which permits use, sharing, adaptation, distribution and reproduction in any medium or format, as long as you give appropriate credit to the original author(s) and the source, provide a link to the Creative Commons license, and indicate if changes were made. The images or other third party material in this article are included in the article's Creative Commons license, unless indicated otherwise in a credit line to the material. If material is not included in the article's Creative Commons license and your intended use is not permitted by statutory regulation or exceeds the permitted use, you will need to obtain permission directly from the copyright holder. To view a copy of this license, visit <http://creativecommons.org/licenses/by/4.0/>.

© The Author(s) 2021